ABSTRACT

Title of thesis: A SIMPLIFIED MODEL OF PLANETARY CHEMICAL VAPOR DEPOSITION REACTORS

Negin Shahshahan, Master of Science, 2009

Directed by: Professor Raymond A. Adomaitis
Department of Chemical and Biomolecular Engineering

A simplified model for planetary chemical vapor deposition reactors is proposed and used to compute deposition species mole fraction and deposition rate in the reactor depletion zone. First, the modeling and optimization work performed in the literature is reviewed and their representative deposition rate profiles are extracted. Afterwards, several simplifying assumptions are applied to derive the reactor modeling equation, and the eigenfunction expansion solution is subsequently computed using a previously developed MATLAB object-oriented computational framework. The simulation result for the deposition profile is improved by modifying the inlet boundary condition, and is then compared with the previously published profiles. The MATLAB optimization toolbox is used to find the optimal deposition profile giving the best match with the published, detailed simulator profiles. Finally, an evaluation of the model consistency with the published results is given.

A SIMPLIFIED MODEL OF PLANETARY CHEMICAL VAPOR DEPOSITION REACTORS

by

Negin Shahshahan

Thesis submitted to the Faculty of the Graduate School of the
University of Maryland, College Park in partial fulfillment
of the requirements for the degree of
Master of Science
2009

Advisory Committee:
Professor Raymond A. Adomaitis, Chair/Advisor
Professor Sheryl Ehrman
Professor Panagiotis Dimitrakopoulos

Acknowledgments

I would like to express my deep gratitude to my advisor, Professor Raymond A. Adomaitis, for all his help and support. His constant advice and guidance throughout this work is greatly acknowledged. I am also grateful to him for helping me understand his developed computational framework which was extensively used in this work. I would also like to thank Professors Ehrman and Dimitrakopoulos for accepting to serve on my thesis committee, and for their valuable suggestions and opinions.

Table of Contents

List of Tables

List of Figures

Chapter 1

Introduction to Planetary Reactor Systems

Chemical vapor deposition (CVD) is an important technique for epitaxial growth of a wide range of compound semiconductors. Among various types of CVD processes, metalorganic vapor phase epitaxy (MOVPE) is the principal method used to grow single-crystalline layers of semiconductor materials. A variety of reactor configurations may be used in chemical vapor deposition for thin-film semiconductor processing depending on the physical properties of the material system and the nature of the gas-phase reactions taking place. The multi-wafer planetary reactor is a well-known reactor system which consists of multiple wafers (substrate) that undergo a planetary-like rotation around the center of the reactor. In this design, reactant gas flows radially outward from a central inlet nozzle over the susceptor containing the wafers, each of which rotates on its individual axis. A schematic view of these reactors is shown in Fig. 1.1. The main characteristic of this design is the elimination of reactor-induced angular non-uniformity through susceptor rotation and reduction of the intrinsic effect of gas phase reactant decomposition and precursor depletion in the gas phase through wafer rotation [12].

In the planetary reactor system, the precursors are usually fed through a split-feed inlet nozzle near room temperature. The gas precursor is carried at a low concentration level in a carrier gas that has no effect on the reactions taking place

during the deposition process. One or more of the precursors undergoes gas-phase thermal decomposition through a sequence of irreversible reactions which produce gas phase species capable of deposition. The reactor is operated at such a high temperature that the deposition is mass-transfer limited, and thus the reactant gas concentration plays an important role in the deposition rate [13].

As an example, the common precursors for SiC growth are silane (SiH_4) and propane (C_3H_8), with hydrogen as the carrier gas. A reaction mechanism which describes gas-phase decomposition of these precursors is used for the reaction-kinetic model [10]. The SiC formation can be represented by the following reaction sequence for silane: $SiH_4 \rightarrow SiH_2 \rightarrow Si$, which produces silicon atom responsible for the film growth. Likewise in GaN deposition, for the commonly used precursors trimethylgallium ($(CH_3)_3Ga$) and ammonia (NH_3), the sequence of reactions that TMG undergoes is: $TMG \rightarrow DMG \rightarrow MMG \rightarrow Ga$, in which the two species produced by thermal decomposition of TMG and DMG (dimethylgallium), i.e. Ga and MMG (monomethylgallium), are capable of deposition onto the wafer surface [9].

The planetary reactor can be split up into three distinct regions of reactor operation along the radial direction. The first region is the central zone where the reactants heat quickly to reach the high temperature required for the process. In the second zone of the reactor a sequence of gas phase reactions commence which produce the gas species capable of deposition, as diccussed above. In this region there is an increasing deposition rate due to the ongoing gas phase reactions. The third region begins after the peak deposition rate, where the species involved in

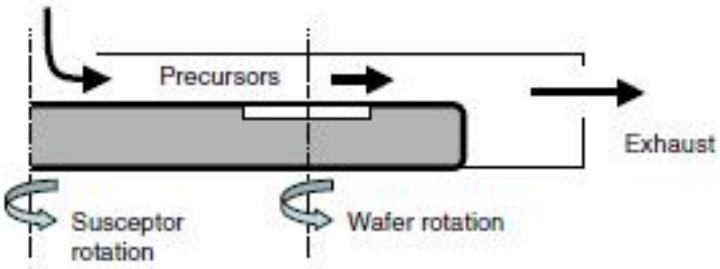

Figure 1.1: Cross-sectional view of a planetary reactor

gas phase reactions have been depleted and only those responsible for film growth remain. Therefore, in the third region often referred to as depletion zone, there is a radial deposition profile that tapers off with increasing radius [12]. The reactor operating parameters are usually set so that the wafer is located in the depletion zone.

Multi-wafer planetary reactors are widely used growth systems and are especially suitable for large scale production due to the high degree of growth rate uniformity and process reproducibility [1]. However, wafer rotation alone does not guarantee acceptable film uniformity and further optimization of process operating parameters is required.

1.1 Objective

Various simulation studies have described the use of physically based models to identify operating conditions that result in uniform films under wafer rotation. Generally, these studies include detailed, two-dimensional steady-state models of reactor heat transfer, reactant gas flow and chemical species reaction and transport

[12]. The results are often compared to experimental data to verify the validity of the model.

The detailed models developed have a high level of comlexity that is often more than required for the optimization studies of the system. The need for a simplified model which is capable of determining the deposition rate profile with a lower computational cost is strongly felt. The purpose of this study is to develop a simple model which determines the operating parameters integral to the deposition process, and enables us to achieve more uniform growth rates by adjusting the design and operating parameters verified by the model.

Chapter 2

Planetary Reactor Survey

There have been numerous detailed studies on the numerical modeling and simulation of planetary reactors, and various approaches have been used to achieve uniform films inside the reactors. Bergunde, et al. [1] developed a model for predicting the temperature distribution in a multiwafer planetary reactor, and used it to achieve higher growth rate uniformity. Jurgensen, et al. [2] used mathematical modeling to study MOCVD reactors and predict growth rate distributions. Bergunde, et al. [3] studied the dependence of the growth rate profiles on flow parameters, reactor pressure and growth temperature both experimentally and theoretically. Beccard, et al. [4] described the use of high temperature CVD reactors to grow SiC and nitrides, and used extensive modeling to obtain uniformity optimization. Brien, et al. [5] discussed modeling and simulation of MOVPE growth of thin films and the choice of process parameters. Burk, et al. [6] presented the experimental results for SiC epitaxial growth employing a unique planetary reactor. Karpov [7] reviewed the recent advances in the modeling of MOVPE of various compounds. Dauelsberg, et al. [8] presented the modeling and experimental studies of $Ga_{1-x}In_xP$ and identified the mechanisms governing growth rate uniformity. Parikh and Adomaitis [9] performed an extensive study on the gallium nitride growth chemistry and the effect of reactor geometry on deposition kinetics in a planetary CVD system. Moreover, Parikh and

Adomaitis [9] and Parikh, et al. [10] developed a geometrically based uniformity criterion for film uniformity control in a planetary reactor and studied the reactor operating conditions that most influence uniformity. Martin, et al. [11] investigated the modeling and subsequent experimental validation of GaN and InGaN growth processes in both closed coupled showerhead reactor and planetary reactor. And finally Lundin, et al. [19] carried out experimental and modeling study of GaN for a single-wafer horizontal reactor and for a multiwafer planetary reactor.

2.1 Modeling

Bergunde, et al. [1] studied the temperature distribution in a multiwafer Aix-2000 planetary reactor for (Al,Ga)As growth. The mathematical model used was based on the two-dimensional solution of coupled partial differential equations describing conservation of total mass and momentum, heat transfer and the chemical species' convective and diffusive mass transport in the gas mixture. To predict the temperature distribution in the reactor, heat transfer calculations assuming non-grey radiative transfer through a non-participating medium and partitioning of the thermal radiation wavelength spectrum into a series of finite bands were employed. The numerical scheme involved a finite volume method using block-structured non-orthogonal collocated grids for two-dimensional model, while convergence speed-up was achieved by employing a multigrid technique.

Jurgensen, et al. [2] used a planetary reactor for the MOCVD of GaN which requires relatively high process temperatures. The flow, concentrations and the tem-

peratures in the reactor were predicted using the numercial solution of the Navier-Stokes equations coupled with heat transfer and mass transport of key chemical species. The model also included homogeneous and heterogeneous chemical reactions. In the modeling of radiative heat transfer, multi-band grey-diffusive radiation exchange between solid boundaries in the reactor was employed. The wavelength dependence of the optical properties also was included in the model. Moreover, it was assumed that the mass transport of the decomposition products to the growing layer controls the growth rate.

Bergunde, et al. [3] investigated the dependency of GaAs and AlGaAs growth rate profile and composition on flow parameters, reactor pressure and growth temperature in an Aix-2000 planetary reactor. The calculations were based on a two-dimensional diffusion model using a coupled set of equations for simulation of flow, heat transfer and mass transport of the species. The results showed that while the assumption of diffusion limited growth is correct for the bulk of the reactor, kinetic limitations may not be neglected in the inlet region.

Beccard, et al. [4] studied the epitaxial growth of SiC and GaN films in a family of high temperature reactors. Their two-dimensional model showed that the gas phase in the reactor is laminar and stable. The modeling approach of Brien, et al. [5] was based on the solution of mixed convective laminar flow of multi-component gas mixtures, coupled with heat and mass transfer. They implemented a standard computational fluid dynamics (CFD) technology to solve the model and also computed the heat transfer by thermal radiation by means of a Monte Carlo ray tracing approach.

Karpov [7] suggested a quasi-thermodynamic (QTD) approach in which the atoms in the adsorption layer are in equilibrium with the crystal bulk. In this approach the only growth limiting surface reaction is treated kinetically, and the other are assumed to proceed under equilibrium conditions. The growth model Dauelsberg, et al. [8] applied, assumed non-competing incorporation of In and Ga into the growing epitaxial layer at mass transport limited growth conditions. The kinetically limited deposition on the heated quartz walls was also taken into account.

In a study focused on defining uniformity modes and the nearest uniformity producing profile, Parikh, et al. [10] developed a detailed two-dimensional transport and reaction-kinetic model for a planetary SiC CVD reactor. The system of nonlinear partial differential equations obtained from fundamental momentum, heat and mass transfer equations, was discretized by collocation and solved by implementing the Newton-Raphson method. Parikh and Adomaitis [9] developed a similar 2D model as well as a simplified 1D model for epitaxial GaN growth and showed that the two models match well.

The modeling approach Martin, et al. [11] performed was based on the solution of a mixed convective laminar gas flow coupled with heat transfer using the computational fluid dynamics (CFD) multi-physics software package CFD-ACE+, together with an advanced reaction chemistry module. Lundin, et al. [19] performed a simulation of GaN growth by means of the CVD-Module computational tool and applied a surface chemistry model in addition to the modeling of the flow of the reacting mixture, heat transfer and gas-phase chemical reaction mechanism.

2.2 Uniformity Optimization

Bergunde, et al. [1] varied the temperature of the reactor ceiling by changing the composition of a H_2/Ar ceiling cooling gas mixture and the thermal coupling to the water-cooled top of the reactor. Moreover, the temperature profile was locally varied in the central area of the reactor by adjusting the heat flux density from the IR-heater unit. It was found that changes in the reactor temperature field directly affect the growth rate distribution on the susceptor. It was concluded that an optimized temperature distribution minimizes the formation of reactor wall deposits and results in high growth rate uniformity of the deposited films.

Jurgensen, et al. [2] observed that total pressure reduction does not change the growth rate significantly. The total flow rate and the ratio of the two flows entering the reactor through a two-flow inlet nozzle were used to optimize both growth rate and uniformity. Uniformity was improved by replacing H_2 with N_2 with a lower flow rate as the carrier gas. Higher growth rates were obtained by adjusting a higher molar flow of the precursors in the reactor.

To obtain stable growth conditions, Bergunde, et al. [3] minimized the deposition on the reactor ceiling by adjusting the ceiling temperature. It was shown that the total flow rate and the ratio of the upper to the lower inlet flow affect the growth rate profile. The position of the maximum and the downstream depletion slope of the rate profile could be changed, and tuned to yield high growth rate homogeneity. A change in growth temperature necessitated again a fine-tuning of the flow rates. Also, lower operating pressures were found more preferable for obtaining

homogeneous growth. Furthermore, a change in the reactor inlet geometry enabled the growth of highly homogeneous layers.

In the AIX 2000/2400 CVD planetary reactor of Beccard, et al. [4], the temperature was controlled by adjusting the gas composition between the ceiling and the water cooled reactor top. It was observed that higher TMGa flows yield higher growth rates, while temperature affects the film uniformity. Simulation also showed how to optimize the reactor geometry to guarantee high quality deposition.

Brien, et al. [5] carried out the uniformity tuning by the total flow rate of process gases into the process volume. They found that the steepness of depletion is reduced with increasing total flow. Therefore, they concluded that the value of the total flow rate and the ratio of flow rates between upper and lower inlets were the dominant factors in thickness uniformity. Burk, et al. [6] showed that doping and thickness nonuniformity correlate with the total variation in susceptor temperature. Dauelsberg, et al. [8] found that the growth rate at kinetically limited conditions decreases at lower pressures, while diffusion limited growth is not affected significantly by pressure.

Parikh, et al. [10] tested the growth rate results obtained from simulation against experimental data and found good agreement between the two profiles. It was found that an increase in flowrate improved SiC film uniformity, which is attributed to the effect of higher total flowrate on reducing reactor residence times and pushing the peak of the deposition rate profile closer to the nearest uniformity producing profile. Parikh and Adomaitis [9] concluded that the extent to which the competing reaction pathways occur is a function of reactor geometry, operat-

ing conditions and the degree of precursor mixing. Uniformity optimization based on the nearest uniformity producing profile approach showed that uniform films of gallium nitride can be produced by decreasing the susceptor temperature and the total fowrate.

To scale up from the more conventional $24 \times 2"$ to the $42 \times 2"$ planetary reactor configuration, Martin, et al. [11] developed a new gas injector design for III-nitride growth. A third inlet for the supply of group V species was introduced above the NH_3 and group III inlets, which pulled the depletion curve peak further upstream due to the shortening of the gas entrance length. The ratio of the gas flows through the upper and lower group V inlets was used as a tuning parameter for the layer thickness uniformity by varying the position of the depletion curve peak.

The experiments Lundin, et al. [19] performed in the AIX2000HT planetary reactor showed that at a constant residence time, the growth rate significantly increases with pressure, which is attributed to longer diffusion times characteristic. However, at a constant pressure, the growth rate strongly decreases with the residence time mainly due to the parasitic deposit formation on the reactor ceiling.

To summarize, both reactor design and operating conditions can affect film growth rates and film thickness and composition spatial uniformity. In terms of operating conditions, it was found that carrier gas flow rate, precursor concentration, reactor temperature and total pressure all affect film growth rate and uniformity.

2.3 Deposition Plots

A MATLAB script is written to extract data points from the deposition rate profiles which were computed using detailed simulations in the cited papers. getplotdata.m uses MATLAB functions to read the plots in jpeg format into MATLAB and to select points from the figure using the mouse, resulting in the coordinates of data points as the output. This allows us to plot growth rate as a function of radial distance for simulation results individually and accurately (Figs. 2.1-2.8). The radial distance from the center of the reactor in which the peak deposition rate is observed is indicated by R_0. In other words, R_0 can be described as the gas inlet section radius and its value depends on the reactor geometry as well as the operating parameters.

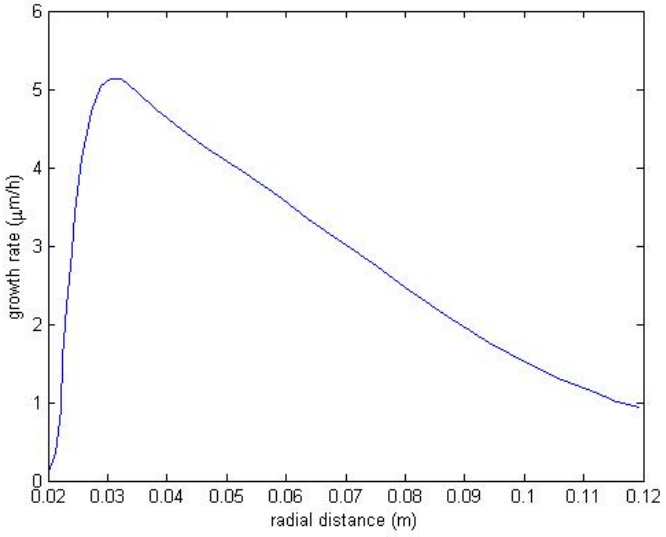

Figure 2.1: Calculated GaAs growth rate profile for 40% cooling gas composition; Bergunde et al. [1], $R_0 = 0.0323$ m

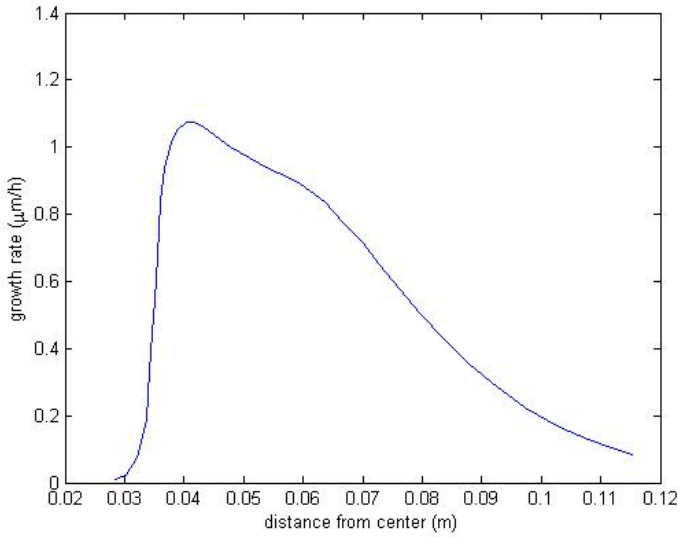

Figure 2.2: Calculated growth rate distribution with N_2 carrier gas and total flow 2.5 l/min; Jurgensen et al. [2], $R_0 = 0.0415$ m

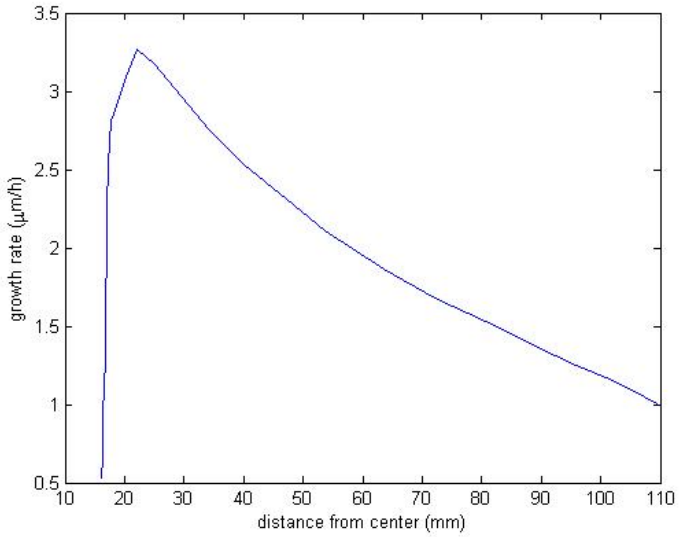

Figure 2.3: Calculated growth rate profile for total flow rate = 17.2 slm; Bergunde et al. [3], $R_0 = 22.1795$ mm

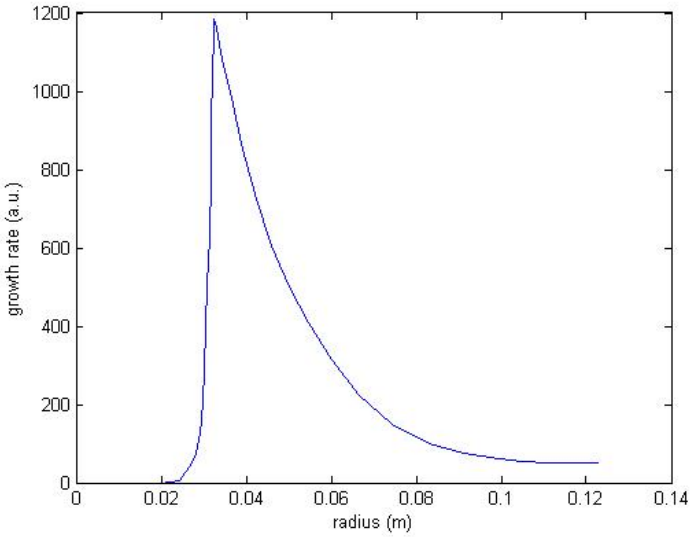

Figure 2.4: Simulation of SiC growth, AIX 2000HT for 4.3 (nl/min) H_2 carrier gas; Beccard et al. [4], $R_0 = 0.0323$ m

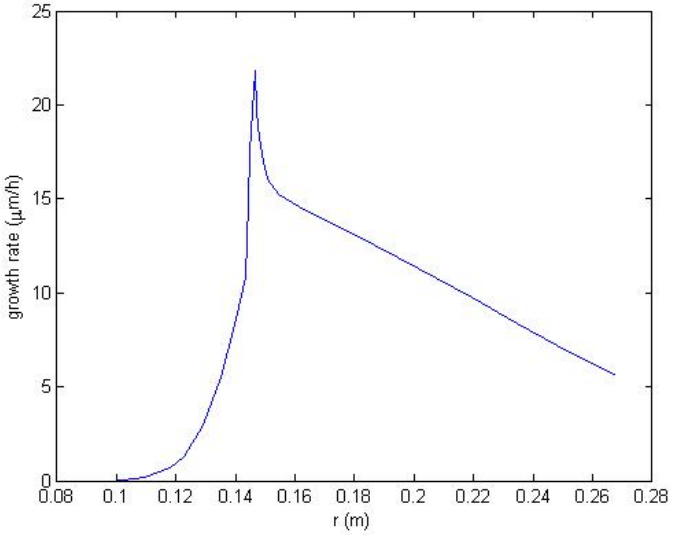

Figure 2.5: Predicted GaP growth rate profiles for flow rate = 35 slm; Brien et al. [5], $R_0 = 0.1466$ m

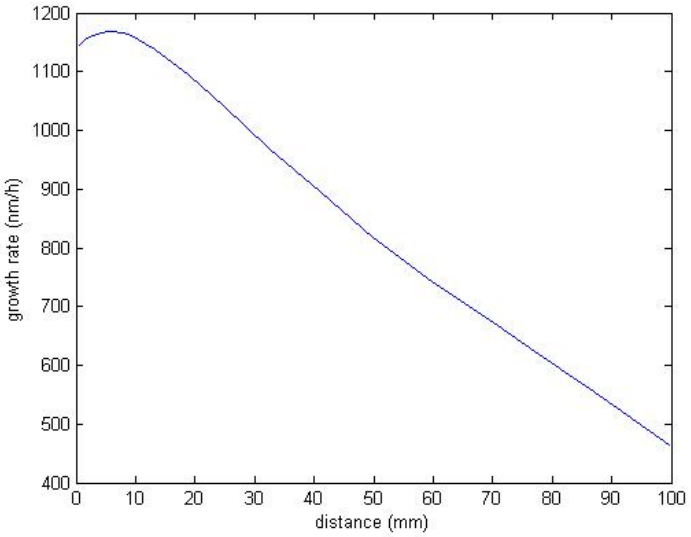

Figure 2.6: Modeling of InGaP MOVPE in the AIX-2400 planetary reactor; Karpov [7], $R_0 = 6.3764$ mm

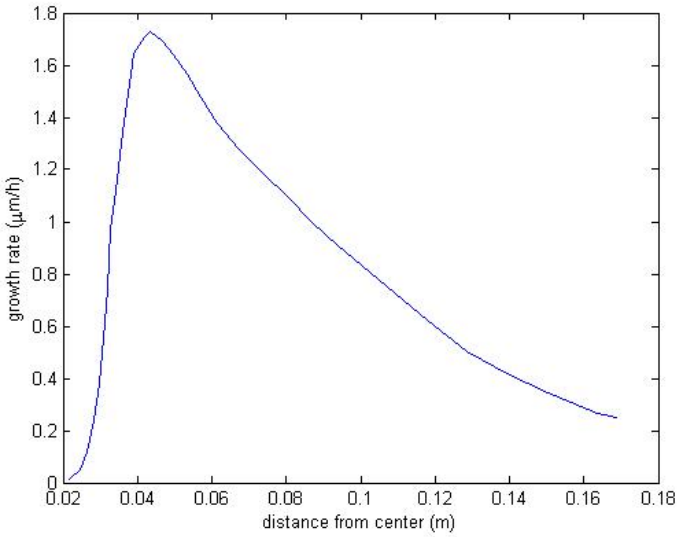

Figure 2.7: Calculated growth rate distribution of GaInP in AIX 2400G3 at total flow rate Q=12 slm; Dauelsberg et al. [8], $R_0 = 0.0433$ m

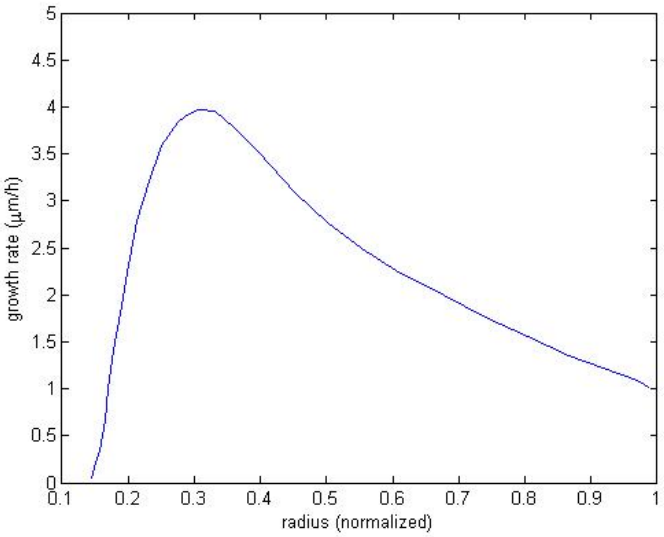

Figure 2.8: GaN Growth rate as a function of susceptor radius in a planetary reactor with triple gas injector; Martin et al. [11], $R_0 = 0.3069$

Chapter 3

Model Derivation

A common characteristic observed in all figures in the previous chapter is that after R_0, the deposition plots appear like depletion profiles. In the depletion zone of the planetary CVD reactor, no gas-phase reactions take place and the only species left are either those capable of deposition or the non-participating gases that exit the reactor as the exhaust stream. Therefore, after the peak deposition rate, in this region the deposition profile decreases with increasing the radial distance.

The reactor temperature is assumed constant throughout the depletion zone. Moreover, we assume that pressure-induced density variations are negligible, and viscosity, density and all other gas properties are constant with respect to spatial position in this region.

The species conservation equation for the depletion zone in the planetary reactor is derived using a shell balance in the cylindrical coordinate. r is the direction of the flow of the gas phase species, and z is the vertical direction from the wafer surface to the ceiling. The total flux of a gas phase species is a combination of the convective and diffusive fluxes:

$$\begin{aligned} \text{flux in r direction} &= c_i v_r - D_i \frac{\partial c_i}{\partial r} \\ \text{flux in z direction} &= c_i v_z - D_i \frac{\partial c_i}{\partial z} \end{aligned}$$

Because no reaction takes place in the depletion zone, the mass balance equa-

tion reduces to FluxIn - FluxOut (Accumulation equals zero for the steady state condition). Therefore

$$A_r\left[\left(c_i v_r - D_i\frac{\partial c_i}{\partial r}\right)_r - \left(c_i v_r - D_i\frac{\partial c_i}{\partial r}\right)_{r+\Delta r}\right]$$
$$+A_z\left[\left(c_i v_z - D_i\frac{\partial c_i}{\partial z}\right)_z - \left(c_i v_z - D_i\frac{\partial c_i}{\partial z}\right)_{z+\Delta z}\right] = 0$$

where Δr and Δz represent the thickness of the cylindrical shell (differential element). Substituting for the cross sectional areas $A_r = 2\pi r\Delta z$ and $A_z = 2\pi r\Delta r$, dividing the equation by $1/r\Delta z\Delta r$, and taking the limits results in

$$\frac{1}{r}\frac{\partial}{\partial r}\left(c_i r v_r - D_i r\frac{\partial c_i}{\partial r}\right) + \frac{\partial}{\partial z}\left(c_i v_z - D_i\frac{\partial c_i}{\partial z}\right) = 0$$

where c_i is the concentration of species i. The equation can be rewritten in terms of x_i, i.e. the mole fraction of species i

$$\frac{1}{r}\frac{\partial}{\partial r}\left(x_i r v_r - D_i r\frac{\partial x_i}{\partial r}\right) + \frac{\partial}{\partial z}\left(x_i v_z - D_i\frac{\partial x_i}{\partial z}\right) = 0. \tag{3.1}$$

Assuming constant density and viscosity, the Navier-Stokes equation in radial and vertical coordinates together with the continuity equation can be written as

$$\rho\left(v_r\frac{\partial v_r}{\partial r} + v_z\frac{\partial v_r}{\partial z}\right) = -\frac{\partial p}{\partial r} + \mu\left[\frac{\partial}{\partial r}\left(\frac{1}{r}\frac{\partial}{\partial r}(r v_r)\right) + \frac{\partial^2 v_r}{\partial z^2}\right]$$

$$\rho\left(v_r\frac{\partial v_z}{\partial r} + v_z\frac{\partial v_z}{\partial z}\right) = -\frac{\partial p}{\partial z} + \mu\left[\frac{1}{r}\frac{\partial}{\partial r}\left(r\frac{\partial v_z}{\partial r}\right) + \frac{\partial^2 v_z}{\partial z^2}\right]$$

$$\frac{1}{r}\frac{\partial}{\partial r}(r v_r) + \frac{\partial v_z}{\partial z} = 0.$$

To further simplify the model, we assume that the gas flow field is fully developed, the fluid inertial terms are negligible (ρ small), and $v_z = 0$. At normal

CVD conditions, the Reynolds number is usually small and the typical values are < 200, which is compatible with the assumption of negligible inertial (i.e. momentum caused by convection) terms [21]. The equations above reduce to:

$$-\frac{dp}{dr} + \mu\left[\frac{\partial}{\partial r}\left(\frac{1}{r}\frac{\partial}{\partial r}(rv_r)\right) + \frac{\partial^2 v_r}{\partial z^2}\right] = 0$$

$$\frac{1}{r}\frac{\partial}{\partial r}(rv_r) = 0$$

which yield

$$\mu\frac{\partial^2 v_r}{\partial z^2} = \frac{dp}{dr}. \tag{3.2}$$

Given the boundary conditions $v_r(r,0) = v_r(r,h) = 0$, in which h is the ceiling height that is assumed constant, and noticing that the total volumetric flow rate of reactant gas is

$$V = -\frac{1}{6\mu}\pi h^3 r\frac{dp}{dr}$$

the solution to equation (3.2) is:

$$v_r(r,z) = -z(h-z)\frac{1}{2\mu}\frac{dp}{dr} = z(h-z)\frac{3V}{\pi h^3 r}. \tag{3.3}$$

Assuming $x_i r v_r >> D_i r\partial x_i/\partial r$ (i.e. diffusion negligible relative to convection in the radial dimension) and $v_z = 0$, and using the velocity term obtained in (3.3), equation (3.1) reduces to the Graetz problem [14]

$$z(h-z)\frac{3V}{\pi h^3}\frac{1}{r}\frac{\partial x_i}{\partial r} = D_i\frac{\partial^2 x_i}{\partial z^2}$$

subject to boundary conditions

$$x_i(R_0, z) = x_i^o \quad z \in (0, h)$$

$$x_i(r,0) = x_i(r,h) = 0 \quad r \in [R_0, R_P].$$

Refer to Fig. 3.1 for the definitions of R_0, R_P and other notation. The depletion zone is considered to extend from R_0 to $R_S + R_W$, while $R_S + R_W >> h$ based on the typical values presented in [9]. Defining the dimensionless variables

$$\eta = \frac{r - R_0}{R_S + R_W - R_0}, \qquad \zeta = \frac{z}{h} \tag{3.4}$$

together with the Peclet number and dimensionless inlet position parameter for this system

$$Pe = \frac{3Vh}{\pi D_i (R_S + R_W - R_0)^2}, \qquad \eta_0 = \frac{R_0}{R_S + R_W - R_0} \tag{3.5}$$

allows transforming the problem into dimensionless form. Note that the definition of the Peclet number is based on the ratio of the convective and diffusive transport terms. The problem becomes

$$\zeta(1-\zeta)\frac{1}{\eta + \eta_0}\frac{\partial x_i}{\partial \eta} = \frac{1}{Pe}\frac{\partial^2 x_i}{\partial \zeta^2} \tag{3.6}$$

subject to

$$x_i(0, \zeta) = x_i^o \quad \zeta \in (0, 1) \tag{3.7}$$

$$x_i(\eta, 0) = x_i(\eta, 1) = 0 \quad \eta \in [0, 1]. \tag{3.8}$$

This model suggests that the deposition profile depends only on Pe and η_0, which can be adjusted by modifying the reactant gas flow rate and the feed gas (or susceptor) temperature. We will discuss the shape of the inlet profile x_i^o later in this document.

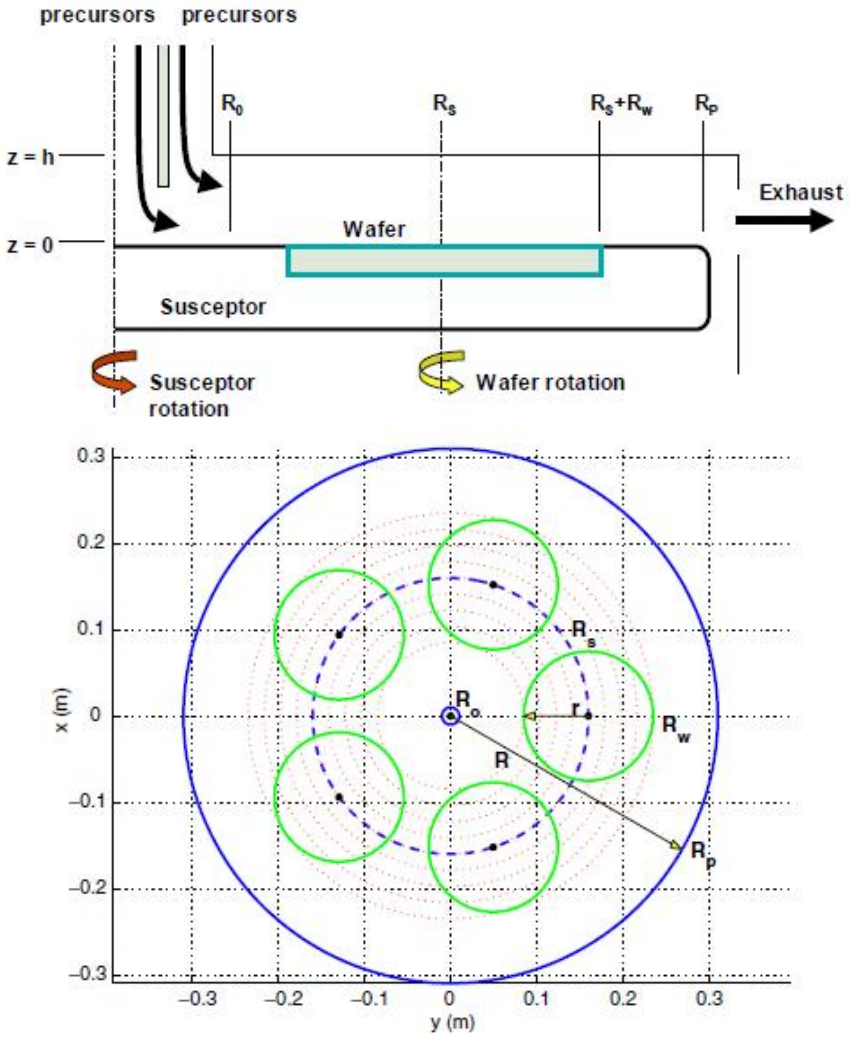

Figure 3.1: Side (upper) and top (lower) views of the geometry of the planetary reactor system

Chapter 4

Eigenfunction Expansion Solution

Equation (3.6) subject to the boundary conditions (3.7-3.8), can be solved using the eigenfunction expansion general solution [12]

$$x(\eta,\zeta)=\sum_{n=1}^{\infty}a_n e^{\lambda_n(\eta+2\eta_0)\eta/2Pe}\psi_n(\zeta) \tag{4.1}$$

where the $\psi_n(\zeta)$ are orthonormal eigenfunctions computed as solutions to the non-self-adjoint eigenvalue problem

$$\frac{d^2\psi}{d\zeta^2}=\lambda\psi\zeta(1-\zeta) \tag{4.2}$$

$$\text{subject to} \qquad \psi(0)=\psi(1)=0$$

and the coefficients a_n are computed using the inlet condition (3.7). Refer to Appendix A for an example of the analytical solution and properties of a non-self-adjoint problem.

4.1 A Simplified Model

Before proceeding to solve the eigenvalue problem (4.2), a simpler case is studied. If in the original two-parameter model (3.6), $\zeta\,(1-\zeta)$ is set equal to one, the following equation is obtained:

$$\frac{1}{\eta+\eta_0}\frac{\partial x}{\partial\eta}=\frac{1}{Pe}\frac{\partial^2 x}{\partial\zeta^2} \tag{4.3}$$

subject to boundary conditions

$$x(0,\zeta) = x^o = 1 \quad \zeta \in (0,1) \tag{4.4}$$

$$x(\eta,0) = x(\eta,1) = 0 \quad \eta \in [0,1] \tag{4.5}$$

The inlet condition considered in (4.4) suggests a constant profile for the inlet mole fraction. In this case the $\psi_n(\eta)$ in the eigenfunction expansion general solution are computed as solutions to the eigenvalue problem

$$\frac{d^2\psi}{d\zeta^2} = \lambda\psi \tag{4.6}$$

$$\text{subject to} \qquad \psi(0) = \psi(1) = 0.$$

The computed normalized eigenfunctions are $\psi_n = \sqrt{2}\sin(n\pi\zeta)$ and the eigenvalues are $\lambda_n = -n^2\pi^2$ for $n = 1, 2, ...$ The inlet boundary condition is used to find the particular solution. If the inlet condition is

$$x(0,\zeta) = \sum_{n=1}^{\infty} a_n\psi_n(\zeta) = 1$$

then the particular solution is:

$$\begin{aligned} a_n &= \int_0^1 \psi_n(\zeta)d\zeta \\ a_n &= \frac{2\sqrt{2}}{n\pi} && \text{(for n odd)} \\ a_n &= 0 && \text{(for n even)} \end{aligned}$$

The results agree with the previously developed Sturm-Liouville problem solver denoted as sl.m function (refer to [15] for a description of the computational method). The first five eigenfunctions are shown in Fig. 4.1.

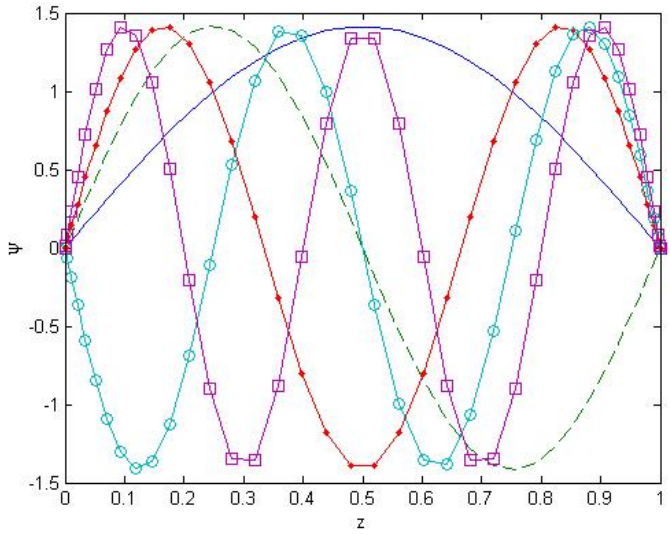

Figure 4.1: First five eigenfunctions for (4.6) computed using sl.m

In this case, the deposition rate is:

$$\delta(\eta) = D\frac{\partial x}{\partial \zeta} = D\sum_{n=1}^{\infty} a_n e^{\lambda_n(\eta+2\eta_0)\eta/2Pe}\frac{d(\psi_n)}{d\zeta} \tag{4.7}$$
$$= D\sum_{n=1}^{\infty} a_n e^{\lambda_n(\eta+2\eta_0)\eta/2Pe}\sqrt{2}n\pi\cos(n\pi\zeta).$$

At $\zeta = 0$ (wafer surface), the deposition rate can be written as:

$$\delta(\eta) = D\sum_{n=1}^{\infty} a_n e^{\lambda_n(\eta+2\eta_0)\eta/2Pe}\sqrt{2}n\pi$$

and so at the gas inlet section radius $\eta = 0$:

$$\delta(\eta = 0) = \sqrt{2}D\sum_{n=1}^{\infty} a_n n\pi$$

Subtituting for a_n yields:

$$\delta(\eta = 0) = 4D\sum_{n\ odd} 1$$

which is a nonconvergent series. In order to overcome this physical inconsistency, the inlet mole fraction is modified to take a parabolic profile similar to the gas flow

field profile. Hence, the inlet condition is changed to:

$$x(0,\zeta) = x^o = 6\zeta(1-\zeta) \quad \zeta \in (0,1) \tag{4.8}$$

The coefficient was determined so that $\int_0^1 x^o d\zeta = 1$ similar to the previous case. Because

$$x(0,\zeta) = \sum_{n=1}^{\infty} a_n \psi_n(\zeta) = 6\zeta(1-\zeta)$$

then the particular solution is:

$$\begin{aligned} a_n &= 6\int_0^1 \psi_n(\zeta)\zeta(1-\zeta)d\zeta \\ a_n &= \frac{24\sqrt{2}}{n^3\pi^3} && \text{(for n odd)} \\ a_n &= 0 && \text{(for n even)} \end{aligned}$$

The results agree with MATLAB sl.m function. In this case, the inlet deposition rate at $\zeta = 0$ is:

$$\delta(\eta = 0) = \frac{48}{\pi^2} D \sum_{n\ odd} \frac{1}{n^2}$$

which is a convergent series and converges to D, i.e. the diffusivity of a gas phase species that contributes to the deposition process. Using the representative values of $Pe = 9$ and $\eta_0 = 0.4993$ (taken from [4]), the simulation result for the deposition species mole fraction (Eq. (4.1)) inside the reactor for the inlet condition (4.4) is shown in Fig. 4.2.

Modifying the inlet condition to (4.8), results in a more uniform profile for the mole fraction shown in Fig. 4.3. Moreover, Fig. 4.4 shows the deposition profile as a function of the reactor radial distance (Eq. (4.7)) on the susceptor, which indicates that the deposition rate (over D) converges to 6 at the start of the depletion zone.

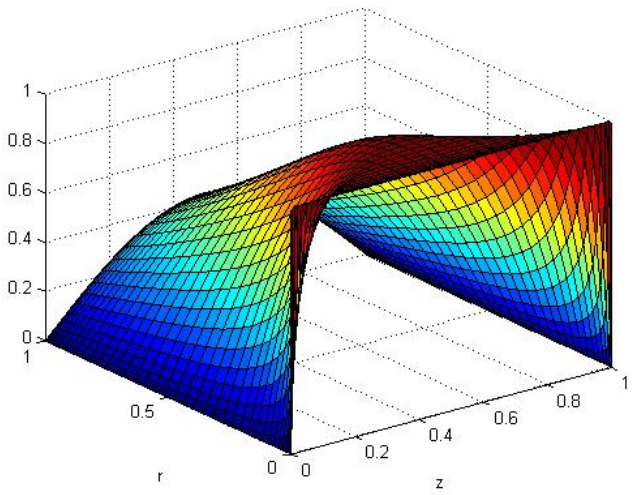

Figure 4.2: Simulation results for the mole fraction obtained from problem (4.3) and inlet condition (4.4)

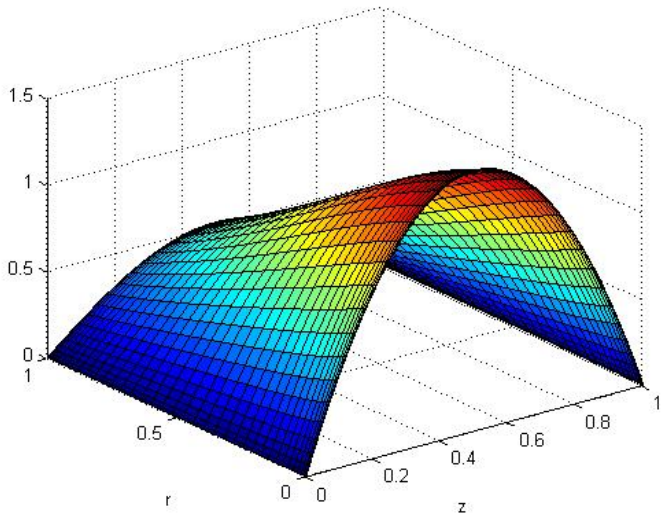

Figure 4.3: Simulation results for the mole fraction obtained from problem (4.3) and inlet condition (4.8)

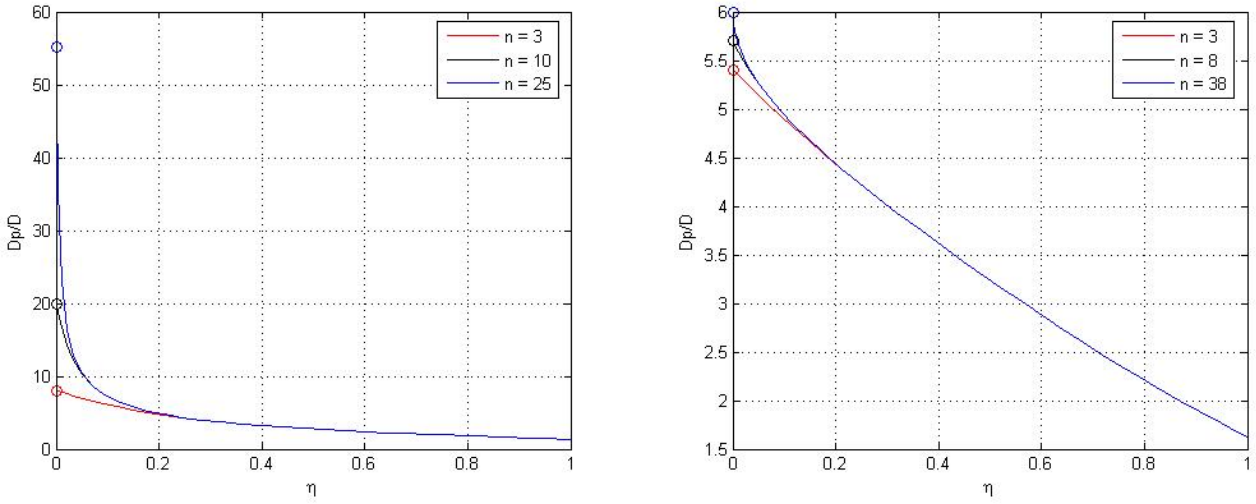

Figure 4.4: Deposition profile as a function of reactor radial distance obtained from (4.3) for $Pe = 9$ and three different truncation numbers; left: inlet condition (4.4); right: inlet condition (4.8)

4.2 Original Model

Now going back to our original problem, the eigenvalue problem (4.2) is numerically solved using sl.m function. The first five eigenfunctions are shown in Fig. 4.5. The orthogonality of the eigenfunctions with respect to the weight function $v = \zeta(1-\zeta)$ can be checked by computing the weighted inner product of the first five eigenfunctions

$$\langle \psi_i(\zeta), \psi_j(\zeta) \rangle_v = \int_0^1 \psi_i(\zeta)\psi_j(\zeta)v(\zeta)d\zeta$$

The computational procedure which uses wip.m is described in the next section and the result is shown below:

w =

1.0000	0.0000	0.0000	0.0000	-0.0000
0.0000	1.0000	0.0000	-0.0000	-0.0000
0.0000	0.0000	1.0000	-0.0000	0.0000
0.0000	-0.0000	-0.0000	1.0000	-0.0000
-0.0000	-0.0000	0.0000	-0.0000	1.0000

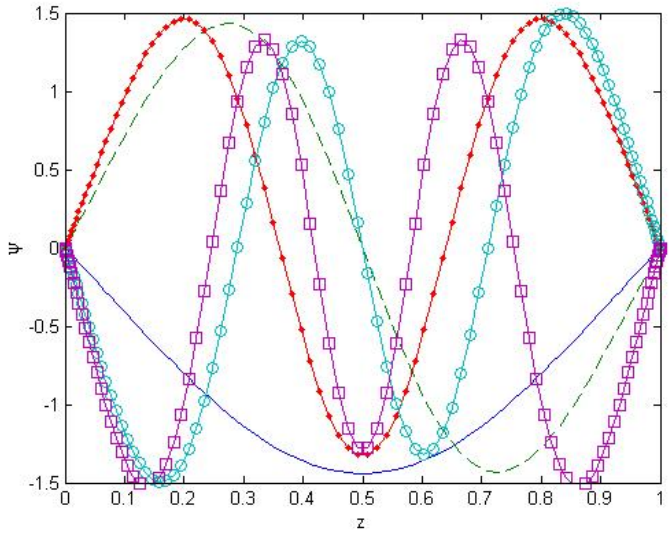

Figure 4.5: First five eigenfunctions for (4.2) computed using sl.m

All off-diagonal elements in the matrix above are zero and the diagonal elements are unity, indicating that the eigenfunctions are orthonormal with respect to the weight function. The particular solution in this case with inlet condition (4.8) is computed using the following relation:

$$a_n = 6 \int_0^1 \psi_n(\zeta)\zeta^2(1-\zeta)^2 d\zeta$$

Fig. 4.6 shows the mole fraction using (3.6) with the initial inlet condition (4.4). Similar to the simplified case, the inlet condition is changed to (4.8) to achieve a uniform mole fraction distribution and convergent deposition rate, shown in Figs. 4.7 and 4.8 respectively.

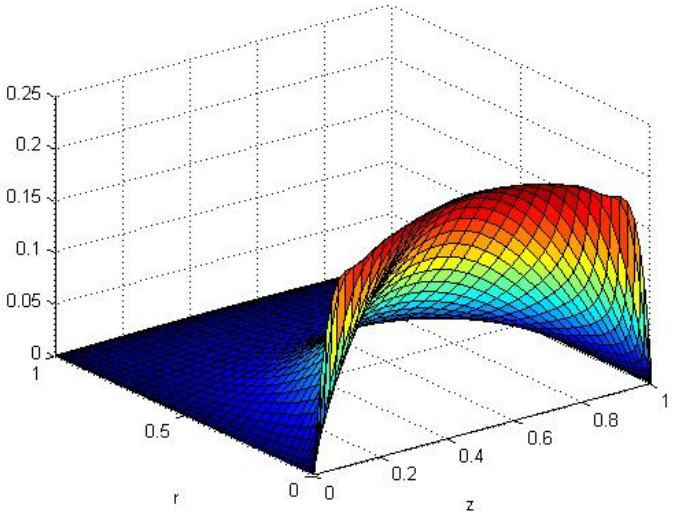

Figure 4.6: Simulation results for the mole fraction obtained from problem (3.6) and inlet condition (4.4)

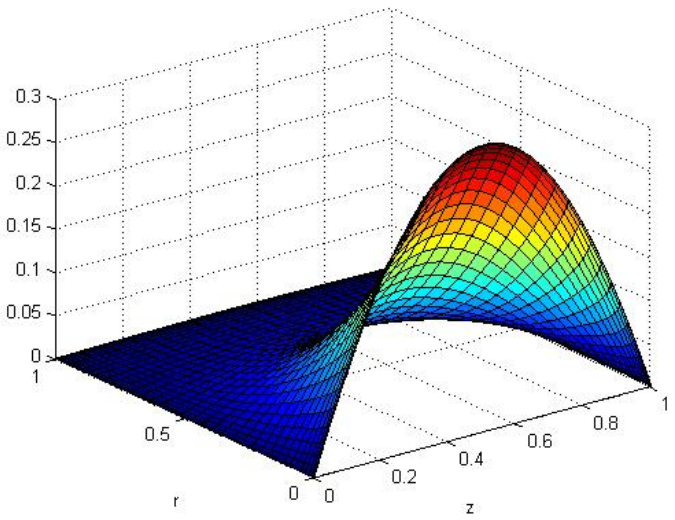

Figure 4.7: Simulation results for the mole fraction obtained from problem (3.6) and inlet condition (4.8)

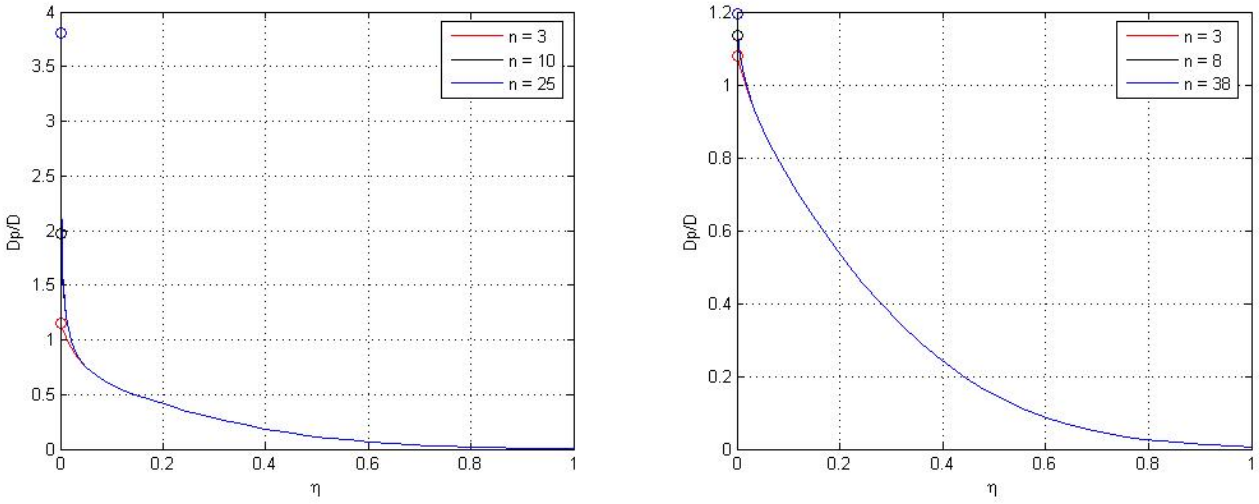

Figure 4.8: Deposition profile as a function of reactor radial distance obtained from (3.6) for $Pe = 9$ and three different truncation numbers; left: inlet condition (4.4); right: inlet condition (4.8)

4.3 Sample Code

The MATLAB object classes and methods used in calculating the eigenfunctions of problem (4.2) and their weigthed inner product are briefly introduced here. Initially a physical domain is defined for our problem using a quadrature grid object constructor.

```
>> Z = quadgrid('slab',40,'z',[0 1]);
```

The next step is to transform the quadrature grid values to scalarfield object to define the weight function specific to this problem.

```
>> s = qg2sf(Z);
```

```
>> v = s*(1-s);
```

sl.m function is then called to compute the eigenvalues and discretized eigenfunctions of the Sturm-Liouville-type problem (4.2) using the boundary conditions and the weight array defined.

```
>> [eval efun] = sl(Z,0,1,0,1,v);
```

In the next step, the eigenfunctions are normalized and wip.m function is utilized to compute the weighted inner product of the first five eigenfunctions. The indices i and j are from 1 to 5.

```
>> enor(i) = efun(i) / sqrt(wip(efun(i),efun(i)*v));
>> w(i,j) = wip(enor(i),enor(j)*v);
```

The final command is used to obtain the matrix shown in the previous section.

Chapter 5

Comparison of the Deposition Profiles

For each of the deposition profiles in Figs. 2.1-2.8, the data points are extracted starting at R_0 and ending with the data point at the largest value of r. $R_s + R_w$ is set to the largest r value which is also assumed to be equal to R_p. The y-axis for each of the sets of data is scaled so that all deposition rates equal 1 at R_0. All of the scaled data are plotted as a function of η (defined in (3.4)), and put on a single graph as shown in Fig. 5.1.

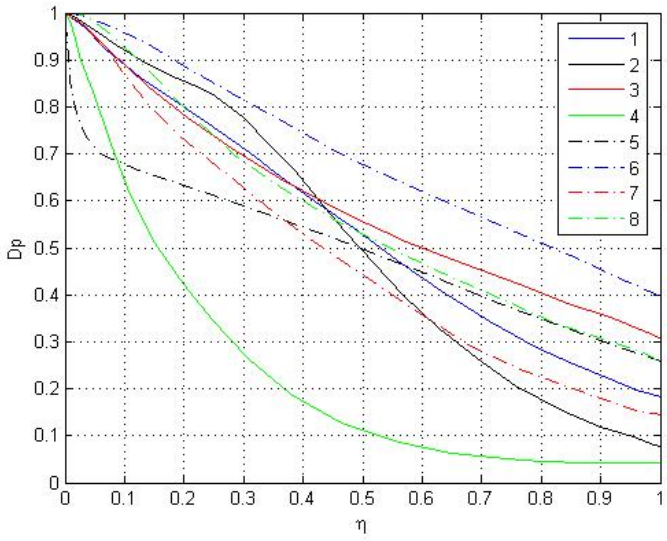

Figure 5.1: Scaled deposition rates as a function of dimensionless radial parameter (numbers in the legend refer to Figs. 2.1-2.8 respectively)

In the next step, we try to find the best Pe number corresponding to each of the obtained curves in Fig. 5.1 which yields the closest match between each set of data and our proposed model. The deposition rate as a function of η was shown in

the right plot in Fig. 4.8, which can be scaled so that the deposition starts from 1 at $\eta = 0$. The modeling equation used in obtaining this plot, Eq. (4.7), depends on values of both Pe and η_0. For each set of data points, η_0 is calculated using (3.5), and our goal is to adjust Pe so that our model (with the highest truncation number) best describes the set of data in each case.

In order to do so, a function is written that takes Pe number as input, computes the corresponding deposition profile based on the presented model, subtracts the deposition profile obtained from the data set from the one predicted by the model (both in scalarfield class), and returns the norm of the difference as the output. The best Pe number for each data set , i.e. the one that yields the minimum norm value, is then calculated using fminunc function from MATLAB optimization toolbox. The optimal Pe can also be obtained by calculating the norm of the difference between the deposition profile extracted from data given in literature and the profile obtained by our model with a range of Pe values, and plotting the norm as a function of Pe number. An example is shown in Fig. 5.2 for curve 1 in Fig. 5.1 which indicates the Pe number that yields the minimum is the optimal Pe. Fig. 5.3 compares the deposition plot corresponding to the data set from [1] with the plot obtained using this optimal Pe number in the model. Figs. 5.4-5.10 show other deposition profiles obtained using the optimal Pe from fminunc for each case together with the deposition data previously extracted and gathered in Fig. 5.1.

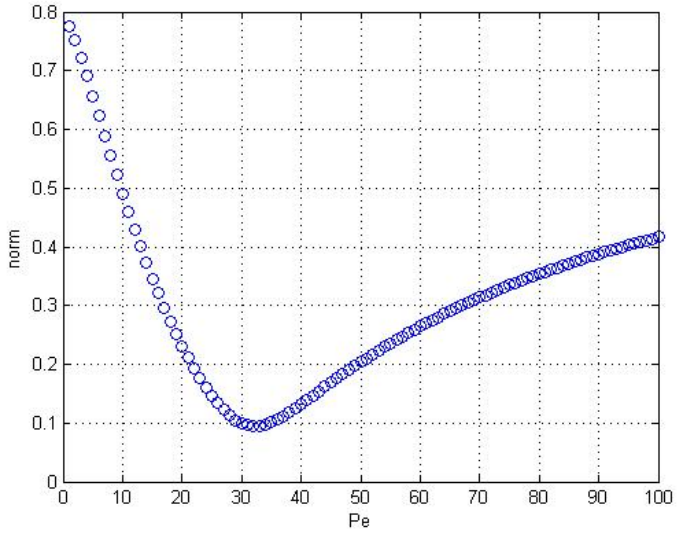

Figure 5.2: Plot of norm of difference between two deposition profiles vs. Pe for curve 1 in Fig. 5.1

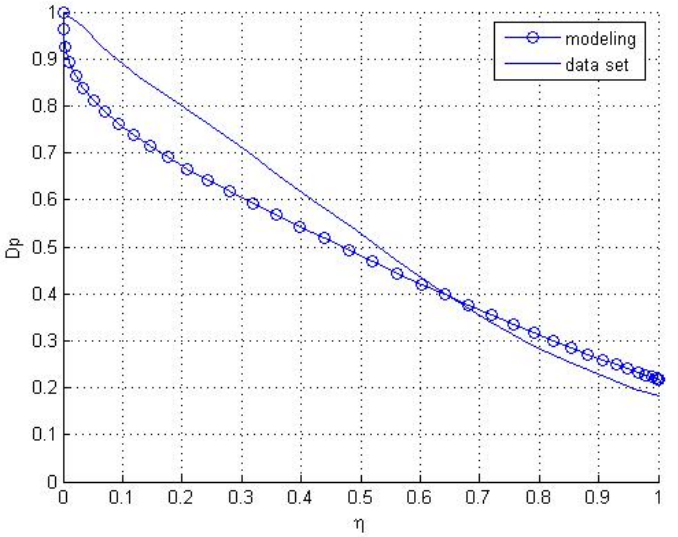

Figure 5.3: Comparison of the scaled deposition rates from curve 1 in Fig. 5.1 and from modeling with the optimum $Pe = 32.19$

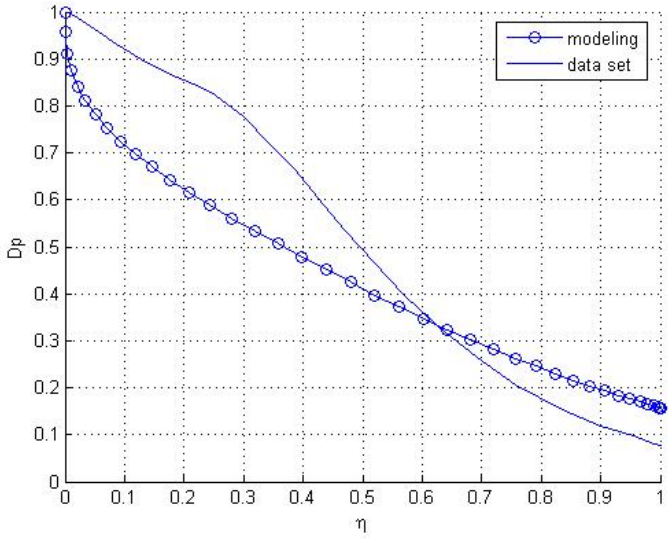

Figure 5.4: Comparison of the scaled deposition rates from curve 2 in Fig. 5.1 and from modeling with the optimum $Pe = 30.92$

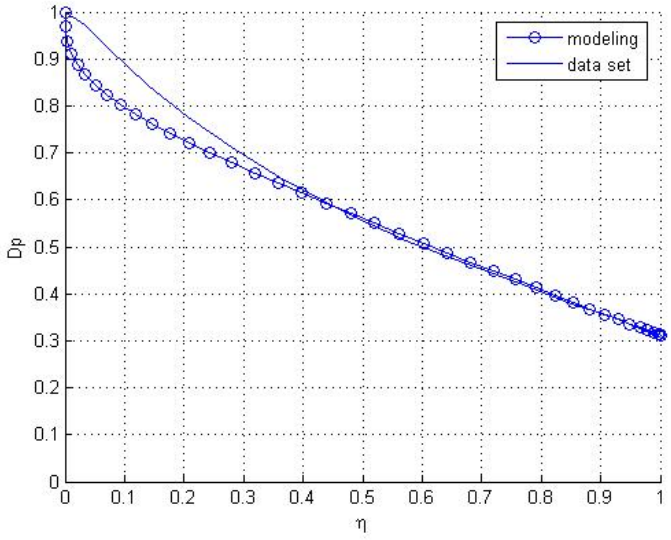

Figure 5.5: Comparison of the scaled deposition rates from curve 3 in Fig. 5.1 and from modeling with the optimum $Pe = 39.40$

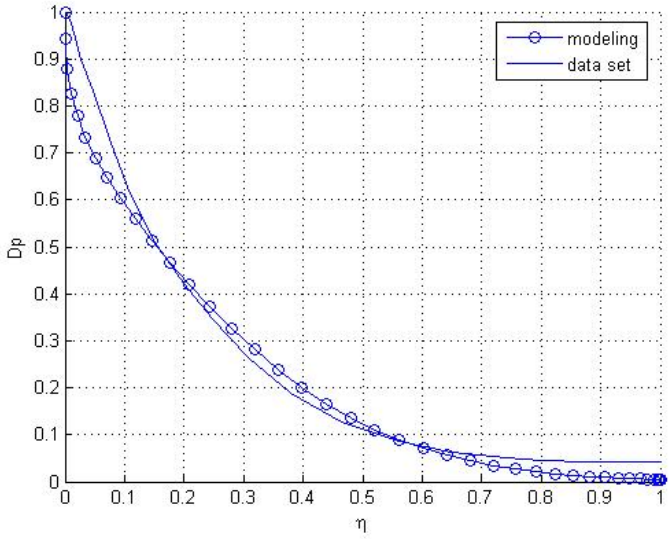

Figure 5.6: Comparison of the scaled deposition rates from curve 4 in Fig. 5.1 and from modeling with the optimum $Pe = 7.63$

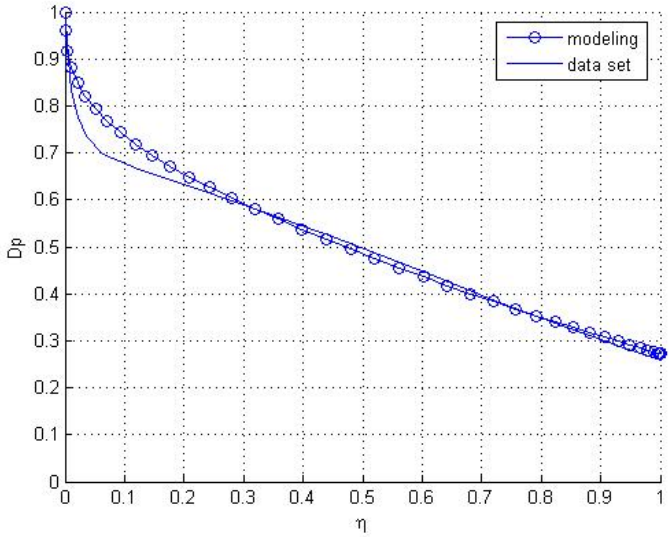

Figure 5.7: Comparison of the scaled deposition rates from curve 5 in Fig. 5.1 and from modeling with the optimum $Pe = 77.49$

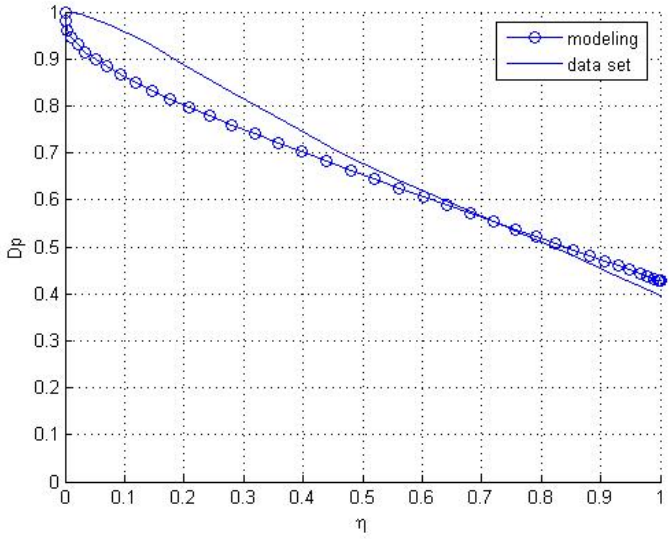

Figure 5.8: Comparison of the scaled deposition rates from curve 6 in Fig. 5.1 and from modeling with the optimum $Pe = 46.47$

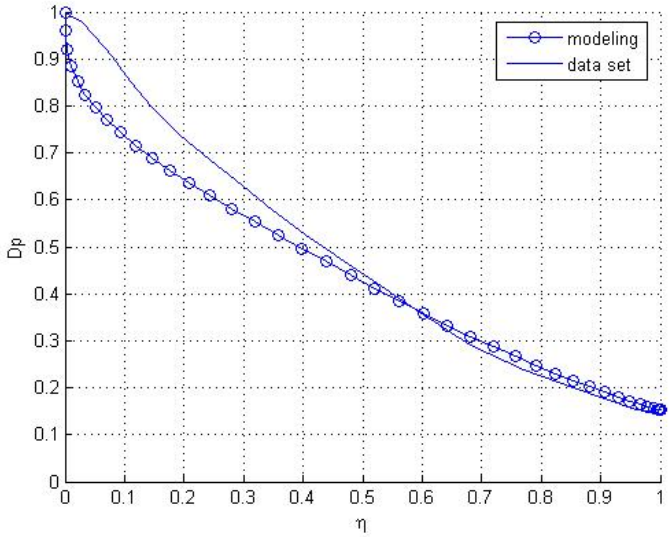

Figure 5.9: Comparison of the scaled deposition rates from curve 7 in Fig. 5.1 and from modeling with the optimum $Pe = 24.10$

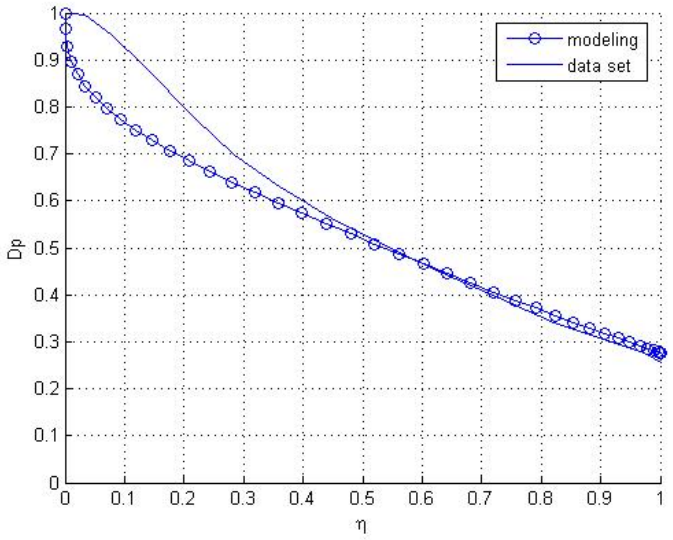

Figure 5.10: Comparison of the scaled deposition rates from curve 8 in Fig. 5.1 and from modeling with the optimum $Pe = 43.62$

Table 5.1 summarizes η_0 values calculated for each set of data in Fig. 5.1, and optimal Pe values found for our model that yield the best deposition profile.

Comparison of the two deposition profiles for each case shows a general agreement between the two plots obtained from the given data and the model with optimal Pe. The common trend observed in almost all the plots is that our developed model is more capable of describing the given deposition profile in the region further away from the start of the depletion zone. In Fig. 5.6, there is a close match over the entire region, which might be due to the extensive modeling used in [4] to find the optimum reactor geometries. On the other hand, Fig. 5.4 shows a poor match between the profiles, which can be attributed to the operating conditions used in [2] that might have delayed the start of the depletion zone in the reactor. Because the data extracted from literature were the results of more detailed simulation studies, the acceptable match between the two deposition rate profiles in each case indicates

Table 5.1: Values of η_0 and optimal Pe corresponding to each deposition plot

curve no.	η_0	Pe
1	0.3721	32.19
2	0.5623	30.92
3	0.2544	39.40
4	0.3569	7.63
5	1.2166	77.49
6	0.0684	46.47
7	0.3456	24.10
8	0.4512	43.62

how successful our simplified model is in replacing those models.

Chapter 6

Conclusion and Future Work

In this work a simplified model for the depletion zone of the planetary chemical vapor deposition reactors was presented. The species mole fraction and deposition rate were computed using a MATLAB object-oriented framework, and the results were compared with the published representative studies. The numerical technique demonstrates a considerably lower computational cost and can be implemented on an ordinary computer, compared to the detailed simulation studies which require significantly higher computational cost.

Simulation results obtained for deposition rate profile suggested that a modification in the inlet boundary condition results in a convergent and physically consistent profile. Therefore, the subsequent comparison of the deposition profiles was performed using the improved model. The two parameters that influence our model, i.e. Pe and η_0, can be adjusted by the gas flow rate and temperature. If our model is considered successful in replacing the more detailed models, these operating parameters critical to uniformity optimization and control can be readily adjusted. The closer a profile is to the depletion profile, the more uniform film is achievable through wafer rotation.

For each pair of the profiles compared, the optimal Pe computed corresponds to a specific gas flow rate which might be different from the flow rate used in the

profile taken from the published results. Besides, calculating an approxiamation to η_0 value in each comparison is based on the extracted data points which do not necessarily yield the true value of radial distances. Furthermore, assigning R_0 to be the start of the depletion zone might not be always accurate, and depending on the process temperature and reactor design parameters, the location of the depletion zone might vary. On the other hand, some of the assumptions made during model derivation might no longer be valid in the specific reactor conditions in some of the previous works which leads to divergent profiles. These justifications might in part prevent our model to match well with the existing profiles.

Despite the reasons above, the acceptable match between the profile pairs in several cases, suggests the capability of our model in obtaining a reasonable deposition profile. Further improvement in the model is still needed to account for the larger error in the starting point of the depletion zone. In the next step of model enhancement, we should focus on model assumptions more compatible with the system under study and try to achieve a balance between model simplification and the complications in reaction kinetics and transport phenomena in the reactor. Particularly, we may have to relax the assumption of no reaction and consider back diffusion for a more reliable result. In terms of simulation performance, replacing slab geometry with cylindrical geometry is under investigation for improving the match in small radial values. Moreover, an attempt to analytically solve the eigenvalue problem that arises in the model and comparison of the analytical and numerical results gives us a better insight into the validity of the performed simulation.

Appendix A

Solution to a Non Self-Adjoint Problem

A.1 Calculation of the Eigenfunctions and Eigenvalues

Consider the non self-adjoint problem [15]:

$$\frac{d^2\psi}{dx^2} - q\frac{d\psi}{dx} - g\psi = \lambda\psi \tag{A.1}$$

subject to boundary conditions:

$$\frac{d\psi(0)}{dx} = 0 \tag{A.2}$$

$$\frac{d\psi(1)}{dx} = 0 \tag{A.3}$$

For this problem we assume that $q = 10$ and $g = 20$. The general form of a Sturm-Liouville problem is [16]:

$$L(\psi) = \frac{1}{\rho(x)}\frac{d}{dx}\left[p(x)\frac{d\psi}{dx}\right] + q(x)\psi$$

By comparing the two equations which are rewritten below

$$\frac{d^2\psi}{dx^2} - q\frac{d\psi}{dx} - (g+\lambda)\psi = 0$$

$$\frac{p(x)}{\rho(x)}\frac{d^2\psi}{dx^2} + \frac{1}{\rho(x)}\frac{dp(x)}{dx}\frac{d\psi}{dx} + q(x)\psi = 0$$

we obtain the equalities:

$$\frac{p(x)}{\rho(x)} = 1 \tag{A.4}$$

$$\frac{1}{\rho(x)}\frac{dp(x)}{dx} = -q \tag{A.5}$$

$$q(x) = -(g+\lambda).$$

Solving (A.5) using (A.4) leads to:

$$p(x) = \rho(x) = e^{-qx}$$

Therefore, the problem becomes:

$$e^{qx}\frac{d}{dx}\left(e^{-qx}\frac{d\psi}{dx}\right) - (g+\lambda)\psi = 0 \tag{A.6}$$

Sturm-Liouville theory [16] tells us that the orthogonality relation is:

$$\int_0^1 e^{-qx}\psi_n(x)\psi_m(x)dx = 0 \quad n \neq m \tag{A.7}$$

Therefore, $\phi_n(x) = e^{-qx}\psi_n(x)$ are the eigenfunctions of the adjoint equation to Eq. (A.6), because in general the system eigenfunctions and their adjoint eigenfunctions are orthogonal

$$\int_0^1 \phi_n(x)\psi_m(x)dx = 0$$

In order to solve equation (A.6), the following substitution is used. This ensures that the new eigenfunctions $w_n(x)$ are orthogonal with respect to a non-weighted inner product.

$$\psi_n(x) = e^{qx/2}w_n(x)$$

This variable transformation reduces the problem into the familiar form of:

$$w_n''(x) - (g + \lambda_n + \frac{1}{4}q^2)w_n(x) = 0 \tag{A.8}$$

$$\frac{dw_n(0)}{dx} = -\frac{q}{2}w_n(0) \tag{A.9}$$

$$\frac{dw_n(1)}{dx} = -\frac{q}{2}w_n(1) \tag{A.10}$$

Assuming a solution of the form

$$\begin{aligned} w_n &= c_1 e^{\alpha_n x} + c_2 e^{-\alpha_n x} \\ \alpha_n^2 &= (g + \lambda_n + \frac{1}{4} q^2) \end{aligned}$$

and using boundary conditions (A.9-A.10), two equations are obtained:

$$\begin{aligned} \alpha_n (c_1 - c_2) &= -\frac{q}{2}(c_1 + c_2) \\ \alpha_n (c_1 e^{\alpha_n} - c_2 e^{-\alpha_n}) &= -\frac{q}{2}(c_1 e^{\alpha_n} + c_2 e^{-\alpha_n}) \end{aligned}$$

The ratio of the left-hand side terms is set equal to the ratio of the right-hand side terms, which after simplification leads to

$$c_1 c_2 e^{-\alpha_n} = c_1 c_2 e^{\alpha_n}$$

Because α_n can not be zero, the equality holds only if either c_1 or c_2 is zero, which using the boundary conditions leads to $\alpha_n = q/2$ or $\alpha_n = -q/2$ respectively. Using the numerical value of q, this means $\alpha_n = \pm 5$. For both cases we obtain $w_n(x) = ce^{-5x}$, and therefore, $\psi_n(x) = c$. The eigenfunctions are normalized with respect to the inner product (A.7):

$$\int_0^1 e^{-10x} \psi_n^2(x) dx = 1$$

which yields the first eigenfunction:

$$\psi_0(x) = \pm \sqrt{\frac{10}{1 - e^{-10}}}$$

and from α_n, the first eigenvalue is:

$$\lambda_0 = -g = -20$$

After considering this special case, the general form of the solution to (A.8) can be written in the form of:

$$w_n = A_n sin\alpha_n x + B_n cos\alpha_n x$$

where

$$\alpha_n^2 = -(g + \lambda_n + \frac{1}{4}q^2) \tag{A.11}$$

Applying boundary conditions (A.9-A.10) yields:

$$\begin{aligned} \frac{A_n}{B_n} &= \frac{-q}{2\alpha_n} \\ \alpha_n(A_n cos\alpha_n - B_n sin\alpha_n) &= -\frac{q}{2}(A_n sin\alpha_n + B_n cos\alpha_n) \end{aligned}$$

When the above equations are combined, we obtain:

$$\left(\frac{q^2}{4\alpha_n} + \alpha_n\right) sin\alpha_n = 0$$

which yields:

$$\alpha_n = n\pi \quad n = 1, 2, ...$$

Note that n can not be zero, because $\alpha_n = 0$ results in $w_n = 0$, which is not a nontrivial eigenfunction. The eigenfunctions take the form:

$$\begin{aligned} w_n &= B_n\left(\frac{-q}{2\alpha_n} sin\alpha_n x + cos\alpha_n x\right) \\ \psi_n(x) &= B_n e^{qx/2}\left(\frac{-q}{2\alpha_n} sin\alpha_n x + cos\alpha_n x\right) \end{aligned}$$

Substituting α_n results:

$$\psi_n(x) = B_n e^{qx/2}\left(\frac{-q}{2n\pi} sinn\pi x + cosn\pi x\right)$$

B_n is calculated to make the eigenfunctions orthonormal to the adjoint eigenfunctions (based on (A.7)):

$$\int_0^1 e^{-qx}\psi_n^2(x)dx = 1$$

$$B_n^2 \int_0^1 \left(\frac{-q}{2n\pi} sinn\pi x + cosn\pi x\right)^2 dx = 1$$

$$B_n = \pm \frac{2\sqrt{2}n\pi}{\sqrt{q^2 + 4n^2\pi^2}}$$

The final form of the eigenfunctions after substituting the numerical values of q and g, is:

$$\psi_n(x) = \pm \frac{2\sqrt{2}n\pi}{\sqrt{100 + 4n^2\pi^2}} e^{5x} \left(\frac{-5}{n\pi} sinn\pi x + cosn\pi x\right) \tag{A.12}$$

and the eigenvalues obtained from (A.11) are:

$$\lambda_n = -(n^2\pi^2 + 45) \quad n = 1, 2, ... \tag{A.13}$$

A.2 Behavior of the Eigenvalues

A theorem on the Sturm-Liouville eigenvalues [17] states that for the SL problem below

$$\frac{d}{dx}\left[p(x)\frac{dy}{dx}\right] - q(x)y + \lambda r(x)y = 0 \tag{A.14}$$

$$\alpha_1 y(a) + \alpha_2 y'(a) = 0$$

$$\beta_1 y(b) + \beta_2 y'(b) = 0$$

if the functions $p(x)$, $p'(x)$, $q(x)$ and $r(x)$ are continuous on the interval $[a, b]$ and that $p(x) > 0$ and $r(x) > 0$ at each point of $[a, b]$, then the eigenvalues, repeated

according to their multiplicity, constitute an infinite sequence of real numbers

$$\lambda_1 \leq \lambda_2 \leq \lambda_3 \leq ...$$

with

$$\lim_{n\to\infty} \lambda_n = +\infty$$

This SL problem is called regular or nonsingular. Moreover, if $q(x) \geq 0$ on [a,b] and the coefficients α_1, α_2, β_1 and β_2 are all nonnegative, then the eigenvalues are all nonnegative.

Now suppose that one of the boundary conditions for a nonsingular SL problem is unmixed, i.e. is in the form of $\alpha_1 y(a) + \alpha_2 y^{'}(a) = 0$. Then every eigenvalue has multiplicity 1 [18]. Under this hypothesis, the eigenvalues satisfy

$$\lambda_1 < \lambda_2 < \lambda_3 < ...$$

instead of the less restrictive inequalities in the theorem.

Now, for our non self-adjoint problem (A.1):

$$\begin{aligned} \frac{d^2\psi}{dx^2} - q\frac{d\psi}{dx} - g\psi &= \lambda\psi \\ \frac{d\psi(0)}{dx} &= 0 \\ \frac{d\psi(1)}{dx} &= 0 \end{aligned}$$

which can be written as:

$$\frac{d}{dx}\left(e^{-qx}\frac{d\psi}{dx}\right) - ge^{-qx}\psi - \lambda e^{-qx}\psi = 0$$

assuming $\lambda^{'} = -\lambda$, by comparison with the general SL problem (A.14), we have:

$$p(x) = e^{-qx}, p^{'}(x) = -qe^{-qx}, q(x) = ge^{-qx} \text{ and } r(x) = e^{-qx}$$

Thus, because the above functions are all continuous, $p(x) > 0$, $r(x) > 0$, $q(x) \geq 0$, and the boundary conditions are unmixed, based on the theorem mentioned earlier, the eigenvalues $\lambda^{'}$ form a nonnegative, infinite sequence of real numbers:

$$\lambda_1^{'} < \lambda_2^{'} < \lambda_3^{'} < ...$$

and therefore the original eigenvalues λ constitute a nonpositive, infinite sequence of real numbers:

$$\lambda_1 > \lambda_2 > \lambda_3 > ...$$

It can be concluded that the eigenvalues of our problem are distinct.

A.3 Orthogonality of the Eigenfunctions

Consider our previous problem (A.6):

$$\begin{aligned} \frac{d}{dx}\left(e^{-qx}\frac{d\psi}{dx}\right) - ge^{-qx}\psi - \lambda e^{-qx}\psi = 0 \\ \frac{d\psi(0)}{dx} = 0 \\ \frac{d\psi(1)}{dx} = 0 \end{aligned}$$

The two solutions ψ_i and ψ_j correspond to distinct values of the eigenvalues λ_i and λ_j, i.e.,

$$\begin{aligned} \frac{d}{dx}\left(e^{-qx}\frac{d\psi_i}{dx}\right) - ge^{-qx}\psi_i - e^{-qx}\lambda_i\psi_i = 0 \\ \frac{d}{dx}\left(e^{-qx}\frac{d\psi_j}{dx}\right) - ge^{-qx}\psi_j - e^{-qx}\lambda_j\psi_j = 0 \end{aligned}$$

Based on the method used in [20], multiplying the first equation by ψ_j and the second by ψ_i and subtracting the two gives

$$\begin{aligned}(\lambda_i - \lambda_j)e^{-qx}\psi_i\psi_j &= \psi_j \frac{d}{dx}\left(e^{-qx}\frac{d\psi_i}{dx}\right) - \psi_i \frac{d}{dx}\left(e^{-qx}\frac{d\psi_j}{dx}\right) \\ &= \frac{d}{dx}\left[e^{-qx}\psi_j\frac{d\psi_i}{dx} - e^{-qx}\psi_i\frac{d\psi_j}{dx}\right]\end{aligned}$$

Integrating over the unit interval gives

$$(\lambda_i - \lambda_j)\int_0^1 e^{-qx}\psi_i\psi_j dx = \left[e^{-qx}\left(\psi_j\frac{d\psi_i}{dx} - \psi_i\frac{d\psi_j}{dx}\right)\right]_0^1$$

Implementing the boundary conditions, the right-hand side of the integrated equation is equal to zero. Therefore

$$(\lambda_i - \lambda_j)\int_0^1 e^{-qx}\psi_i\psi_j dx = 0$$

Because the eigenvalues are distinct, this proves that the eigenfunctions are orthogonal with respect to the weight function e^{-qx}.

Bibliography

[1] T. Bergunde, M. Dauelsberg, L. Kadinski, Yu.N. Makarov, M. Weyers, D. Schmitz, G. Strauch, H. Jergensen, Heat transfer and mass transport in a multi-wafer MOVPE reactor: modelling and experimental studies, *Journal of Crystal Growth* **170** (1997) 66-71.

[2] H. Jurgensen, D. Schmitz, G. Strauch, E. Woelk, M. Dauelsberg, L. Kadinski, Yu.N. Makarov, MOCVD equipment for recent developments towards the blue and green solid state laser, *MRS Internet Journal of Nitride Semiconductor Research*, Vol. 1, Article 26 (1996).

[3] T. Bergunde, D. Gutsche, L. Kadinski, Yu. Makarov, M. Weyers, Transport and reaction behaviour in Aix-2000 planetary metalorganic vapour phase epitaxy reactor, *Journal of Crystal Growth* **146** (1995) 564-569.

[4] R. Beccard, D. Schmitz, E.G. Woelk, G. Strauch, Y. Makarov, M. Heuken, M. Deschler, H. Juergensen, High temperature CVD systems to grow GaN or SiC based structures, *Materials Science and Engineering* B61-62 (1999) 314-319.

[5] D. Brien, M. Dauelsberg, K. Christiansen, J. Hofeldt, M. Deufel, M. Heuken, Modelling and simulation of MOVPE of GaAs-based compound semiconductors in production scale planetary reactors, *Journal of Crystal Growth* **303** (2007) 330-333.

[6] A.A. Burk Jr., M.J. O'Loughlin, H.D. Nordby Jr., SiC epitaxial layer growth in a novel multi-wafer vapor-phase epitaxial (VPE) reactor, *Journal of Crystal Growth* **200** (1999) 458-466.

[7] S.Yu. Karpov, Advances in the modeling of MOVPE processes, *Journal of Crystal Growth* **248** (2003) 1-7.

[8] M. Dauelsberg, L. Kadinski, Yu.N. Makarov, T. Bergunde, G. Strauch, M. Weyers, Modeling and experimental verification of transport and deposition behavior during MOVPE of $Ga_{1-x}In_xP$ in the Planetary Reactor, *Journal of Crystal Growth* **208** (2000) 85-92.

[9] R.P. Parikh, R.A. Adomaitis, An overview of gallium nitride growth chemistry and its effect on reactor design: Application to a planetary radial-flow CVD system, *Journal of Crystal Growth* **286** (2006) 259-278.

[10] R.P. Parikh, R.A. Adomaitis, J.D. Oliver, B.H. Ponczak, Implementation of a geometrically based criterion for film uniformity control in a planetary SiC CVD reactor system, *Journal of Process Control* **17** (2007) 477-488.

[11] C. Martin, M. Dauelsberg, H. Protzmann, A.R. Boyd, E.J. Thrush, M. Heuken, R.A. Talalaev, E.V. Yakovlev, A.V. Kondratyev, Modeling of group-III nitride MOVPE in the closed coupled showerhead reactor and Planetary Reactor, *Journal of Crystal Growth* **303** (2007) 318-322.

[12] R.A. Adomaitis, Uniformity Control in Planetary Chemical Vapor Deposition Reactor Systems, Proceedings of the 17th IFAC World Congress, Seoul, Korea, 2008.

[13] R.A. Adomaitis, The Nearest Uniformity Producing Profile (NUPP) optimization criterion for thin-film processing applications, *Journal of Process Control* **18** (2008) 922-930.

[14] S.T. Hsu, Engineering Heat Transfer, D. Van Nostrand Company, Inc. 1963.

[15] R.A. Adomaitis, Y.-h. Lin, A Collocation/Quadrature-Based Sturm-Liouville Problem Solver, *Applied Mathematics and Computation* **110** (2000) 205-223.

[16] W. Harmon Ray, Advanced Process Control, McGraw-Hill, Inc. 1981.

[17] C.H. Edwards, D.E. Penney, Differential Equations and Boundary Value Problems, Pearson Education, Inc. Third Edition, 2004.

[18] J. Polking, A. Boggess, D. Arnold, Differential Equations with Boundary Value Problems, Pearson Education, Inc. Second Edition, 2006.

[19] W.V. Lundin, E.E. Zavarin, D.S. Sizov, M.A. Sinitsin, A.F. Tsatsul'nikov, A.V. Kondratyev, E.V. Yakovlev, R.A. Talalaev, Effects of reactor pressure and residence time on GaN MOVPE growth efficiency, *Journal of Crystal Growth* **287** (2006) 605-609.

[20] R.A. Adomaitis, Numerical Methods for Chemical Engineers - An object-oriented, MATLAB-based approach, Edition 2.1, 2009.

[21] O. Danielsson, A. Henry, E. Janzen, Growth rate predictions of chemical vapor deposited silicon carbide epitaxial layers, *Journal of Crystal Growth* **243** (2002) 170-184.